Digging Through the Trash: An Investigation into Hidden Sources of Information in GNSS-R Observations

Clara Chew, Margaret Scott, and Ian Colwell

***Abstract*—Interpreting remote sensing data sometimes feels like a dark art. We aim to assign a single meaning to ambiguous signals that were actually affected by a slew of unique conditions. And NASA's Cyclone Global Navigation Satellite System (CYGNSS) data are no exception. When we observe an increase in CYGNSS surface reflectivity, we most often attribute it to either an increase in soil moisture or in inundation extent. Yet distinguishing between these two surface conditions is impossible to do with reflectivity observations alone. Here, we propose a way forward to better understand the primary driver affecting data from CYGNSS and other GNSS-Reflectometry satellites. We present a new metric created using information contained within the surface reflection that is often ignored or discarded during processing, which we label 'little gamma.' We discuss whether this new metric and other such 'coherency metrics' are actually measuring coherency, which is assumed to be indicative of the surface roughness, or whether the story is, in fact, more complicated. Our findings suggest that the dielectric constant of the diffuse component can significantly change a coherency metric with no corresponding change in roughness, and this aspect should be considered when interpreting such a metric. Finally, we present evidence that combining little gamma with surface reflectivity can help us distinguish a change in the observation that is due to soil moisture versus surface inundation, lessening the ambiguity currently plaguing the interpretation of surface reflectivity.**

***Index Terms*—GNSS-Reflectometry, soil moisture, inundation**

I. INTRODUCTION

IN December of 2016, NASA launched Cyclone Global Navigation Satellite System (CYGNSS), the agency's first Earth Venture Class mission. Named because it opportunistically records surface-reflected GNSS signals, the prime objective of this constellation of eight small satellites was to monitor–with a short 7-hour revisit time–ocean surface wind speed during hurricanes and tropical storms [1]. Soon after its launch, however, researchers quickly began exploring other uses of the recorded L-band signals, particularly for land surface applications [2]. In the nine years that CYGNSS has been on orbit, surprising sensitivities of the data to near-surface soil moisture [3]–[10], inundation extent [11]–[15], vegetative biomass and water content [16]–[20], and landscape freeze/thaw state [21]–[23] have been quantified and retrieval algorithms for these variables developed.

Despite the advances made in GNSS-Reflectometry (GNSS-R) during this time, several open questions remain. In particular, CYGNSS data are sensitive to many things, perhaps to *too* many things. How do we know that observed changes in CYGNSS data are due to soil moisture and not due to flooding? How can we distinguish a flat reflecting surface from smooth water? Thus far, the research community's answer to these questions follows one of two approaches: include these confounding variables in a laundry list of potential sources of error, or bring in often imperfect ancillary data to account for them.

Here, we investigate a third approach, in which we explore the potential to use other information contained within the data recorded by CYGNSS to aid in our understanding of the reflecting surface. To this end, we introduce a new metric using CYGNSS data that are often discarded during processing, which we lovingly refer to as 'little gamma,' or γ. We investigate the differences and interplay between this metric and more commonly-derived metrics used for land surface retrievals and what we can learn from those differences. Although the aim of this paper is not to propose new retrieval algorithms, we hope that it will spur further discussion into the underexplored, underutilized, and perhaps misinterpreted information contained within GNSS-R observations.

II. METHODS

A. Calculation of metrics from delay-Doppler maps

For those unacquainted with the GNSS-R data recorded by CYGNSS and other GNSS-R satellites, the fundamental Level 1 observable is a delay-Doppler map, or DDM. Every half second, each CYGNSS satellite records up to four DDMs simultaneously, each one representing a surface reflection that results from a transmitted GNSS signal hitting the surface and reflecting back into space. A DDM is a two-dimensional representation of the cross-correlation of the received signal and a known replica stored within the receiver, each of which is unique to the specific transmitting GNSS satellite. By varying the delay and Doppler shifts during the cross-correlation, DDMs are formed, two examples of which are shown in Figure 1.

Figure 1a typifies a DDM recorded over a topographically flat and smooth surface, such as over calm, inland water or a broad, low-lying valley. The power is concentrated within a small region of the DDM, which stands in contrast to that which is shown in Figure 1b. This DDM would typically

---

C. Chew is with Muon Space, Mountain View, CA, 94043 USA e-mail: clara@muonspace.com

M. Scott is with the University of Colorado, and I. Colwell is with Muon Space.

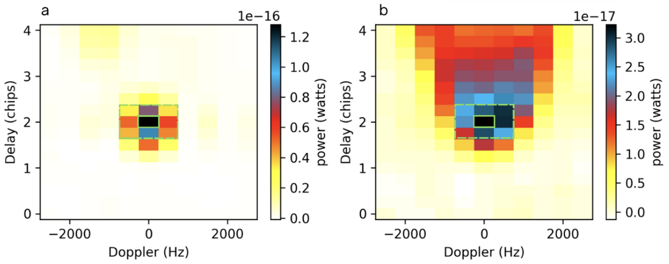

Fig. 1. Two examples of DDMs and how Γ and γ are calculated. Γ is the value of the peak pixel (green solid box), after antenna gain and geometric range corrections. γ is the difference between Γ and the mean value of all eight pixels surrounding the peak (dashed green box) when pixel values are in dB. The DDM in (a) was recorded over inland surface water and (b) was recorded over the open ocean. Note the difference in magnitude between the two colorbars.

Fig. 2. Three raccoons digging through the trash, much like the three authors conducting this research.

result from a reflection recorded over a topographically rough surface, such as from a wind-roughened ocean or mountainous terrain.

It is often convenient to summarize each DDM into a single metric and discard the remainder, and the most common metric for land surface applications is the surface reflectivity.

1) Surface reflectivity (Γ): The peak value of each DDM can be converted into an estimate of the surface reflectivity (Γ). In Figure 1, the peak pixel is denoted by the green solid box. The value within this box is corrected for the effects of the transmitting and receiving antennas, transmitted power, and geometric ranges as in Equation (1), which is the bistatic radar range equation for coherent surface reflections [24]:

$$\Gamma = \frac{P_r(4\pi^2)(R_{sr}+R_{ts})^2}{P_t G_t G_r \lambda^2} \tag{1}$$

where P_r is the received reflected power (i.e., the value of the uncorrected peak pixel), R_{sr} is the range between the specular point and the receiver, R_{ts} is the range between the specular point and the transmitting GNSS satellite, $P_t G_t$ is the effective isotropic radiated power, G_r is the antenna gain of the receiver, and λ is the GPS wavelength (0.19 m). Γ is most often expressed in decibels (dB).

Γ, or a very similar derivative, is commonly used by the CYGNSS community in the retrieval of geophysical variables like near-surface soil moisture or inundation extent (e.g., [5], [13]) and has also been used for biomass and freeze/thaw applications (e.g., [17], [22]). This is because Γ is affected by the dielectric constant of the reflecting surface, which itself is mostly dependent on the amount of liquid water on the surface and in the overlying vegetation [25]. However, Γ is also affected by the roughness of the reflecting surface [26]. There are thus several different variables which could all be affecting Γ simultaneously and to different degrees, which is where the uncertainty in the interpretation of Γ lies.

For the analyses shown here, we will examine how Γ varies in space and time. For spatial analyses, we calculate multi-year averages of Γ using observations from 2020 - 2024 using v3.2 CYGNSS Level 1 files [27]. This five year span was chosen to be after the change from 1 Hz to 2 Hz sampling (July 2019), which shortened the along-track integration period from 7 km to 3.5 km. For analyses of observations within any given grid cell, we use daily averages of observations for the same time period. For all analyses, we grid our observations to a 3-km EASE-2 grid [28] such that if a reported specular reflection point falls within a grid cell, the observation is assigned to that grid cell with no consideration for how far the actual reflection point is from the grid cell center.

Note that although we do not show an example, DDMs can also be corrupted by terrestrial GNSS radio frequency interference (RFI), which affects Γ and other derived DDM metrics. In these situations the data are highly suspect, and we do not consider any grid cells that typically have RFI in our analyses, which we defined as having an average noise value greater than 43.5 dB, a value that comes pre-packaged with the CYGNSS Level 1 files that has been previously shown to correspond with regions of RFI [29]. We do show these regions in our figures, but we have made them semi-transparent.

2) Little gamma (γ): There are other ways of summarizing a DDM than Γ, and here we derive another way, which we will denote as γ. Its calculation is simple: γ is the difference between the peak value of the DDM and the mean value of the eight pixels that surround the peak (i.e., the 3x3 neighborhood of the peak pixel, shown by the green dashed boxes in Figure 1), *after* all pixels of the DDM has been converted from watts to dB:

$$\gamma = P_r - \frac{1}{8} \sum_{\substack{-1 \le m,n \le 1 \\ (m,n) \neq (0,0)}} P(i+m, j+n) \tag{2}$$

where i and j are the row and column indices of the peak pixel, respectively.

A large value of γ means that the peak pixel is large relative to the surrounding pixels. A small value of γ means that the value of the peak pixel is close to that of the surrounding pixels. Although the spatial region represented by these off-specular pixels may be larger than 3 km, for ease of comparison with Γ we also grid γ to 3 km. Future work could conduct sensitivity studies to better quantify the extent of the spatial region represented by γ and how that region varies across space and time.

γ is a quantification of how spread out the power is within each DDM. There are other metrics that also quantify power spread; these are sometimes called 'coherency metrics,' as they are assumed to relate solely to the roughness of the reflecting

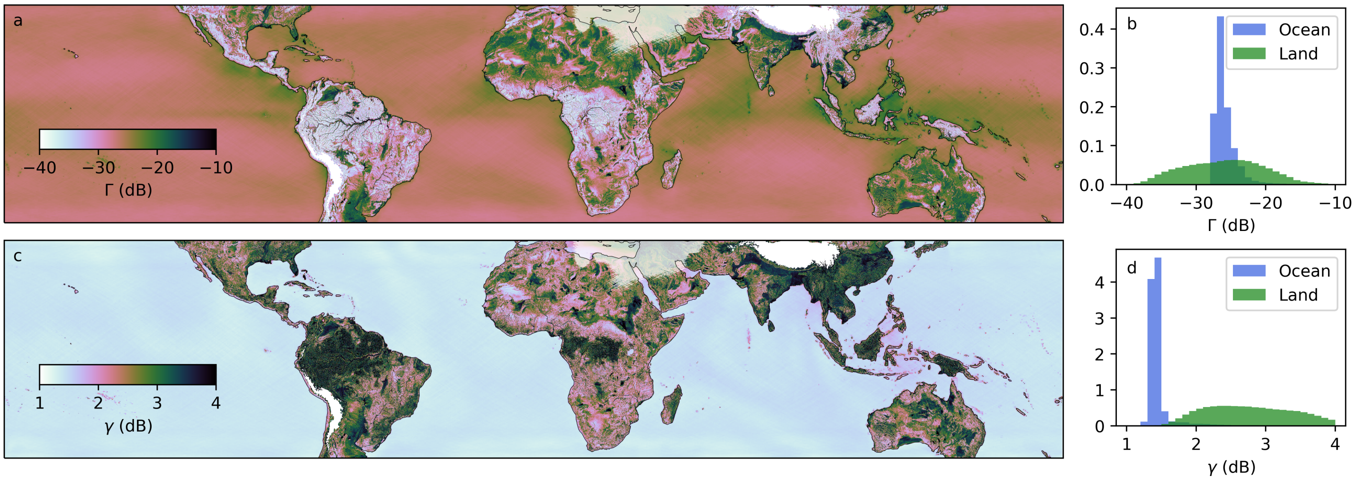

Fig. 3. (a) Long term average (2020 – 2024) of CYGNSS surface Γ. Observations over the ocean were gridded to 36 km, and observations over the land surface were gridded to 3 km. (b) Distributions of (a) binned by land and ocean. (c) Long term average (2020 – 2024) of γ. (d) Distributions of (c) binned by land and ocean. In panels (a) and (c), regions with surface elevation in excess of 3000 m have been removed (i.e., Tibetan Plateau and the Andes Mountains), and regions that experience significant RFI in the Middle East are semi-transparent. CYGNSS data are constrained to +/-38 degrees latitude due to its orbital inclination.

surface and thus how coherent the surface reflection is, which has important implications for the assumed spatial resolution. Examples of coherency metrics include those derived in [11], which analyzes the ratio of the sum of the power from a 3 x 5 ”box” centered on the peak power of the DDM to the sum of the power in the remainder of the DDM, and [30], which analyzes the trailing-edge slope of the waveform. We chose to derive γ instead of examining a different metric of power spread as several other studies have already described the more traditional coherency metrics, and we did not want readers to come to the table with any pre-conceived notions about what they would see. We also wanted the spatial regions affecting our metrics to be as equivalent as possible, which is why we examined a small number of pixels surrounding the peak value. Part of our analysis will question whether a coherency metric is truly measuring coherency, or if the story is more complicated. So let’s get our paws dirty and see what we can learn from these under-explored pixels (Figure 2).

B. *Preparation of ancillary datasets*

In order to understand drivers of any differences between γ and Γ, we need to understand the land surface that characterizes each reflection. To this end we employ several ancillary datasets describing the topography of the land surface, surface water extent, biomass, and near-surface soil moisture. Details of each dataset are described below. All ancillary datasets are gridded to the 3-km EASE-2 grid.

1) Surface water: We generated a static 3-km surface water map using data from the Copernicus Land Monitoring Service (CLMS) where the value of each grid cell indicates the percentage of surface water within that pixel. The CLMS dataset we used is a 100 m global land cover dataset, which provides 23 discrete classifications of land cover from 2019 [31], from which we combined several different water classifications to generate our percentage water map. Although 2019 is outside of our time span of 2020-2024, small differences in water classifications will not significantly affect the bulk analyses shown here. The water classifications that we summed were the Permanent Water Bodies, Herbaceous Wetland, and Ocean classes. This means, for example, that a 3-km grid cell containing 10 percent Permanent Water and 5 percent Herbaceous Wetland would have a value of 15 percent in our static water map. Not only do we quantify how our DDM metrics are affected by surface water, but we also use the map to remove grid cells with greater than 1 percent surface water from consideration when we present analyses of other variables, like topography and biomass. This helps mitigate any sensitivity of DDM metrics to surface water in our investigation of other variables.

2) Digital elevation model: Information about land surface elevation and the topographic roughness of the land surface comes from the Jet Propulsion Laboratory’s Global Digital Elevation Model (JPL GDEM), which is a combination of several different DEMs including the Shuttle Radar Topography Mission (SRTM), the Alaska DEM, Canada DEM, and Global 30 Arc-Second Elevation (GTOPO30). More information about the DEM can be found in [32]. We use this DEM to remove any 3-km grid cell exceeding 3,000 m, which is approximately the upper limit for reflections recorded by CYGNSS. We also use a derivative product of the DEM, which is part of NASA’s Soil Moisture Active Passive (SMAP) ancillary dataset to estimate surface roughness. This derivative is calculated as the standard deviation of elevation within each 3-km grid cell [33]. We convert these roughness values to decibels (dB), as doing so makes for a clearer comparison between topographic roughness and the DDM metrics.

3) Soil moisture: The L-band GNSS reflections that CYGNSS observes are sensitive to soil moisture in the upper 0-5 cm of the soil. This is the same depth as retrieved by the SMAP mission, which is an L-band radiometer launched in 2015 that has a temporal repeat of 2-3 days, depending

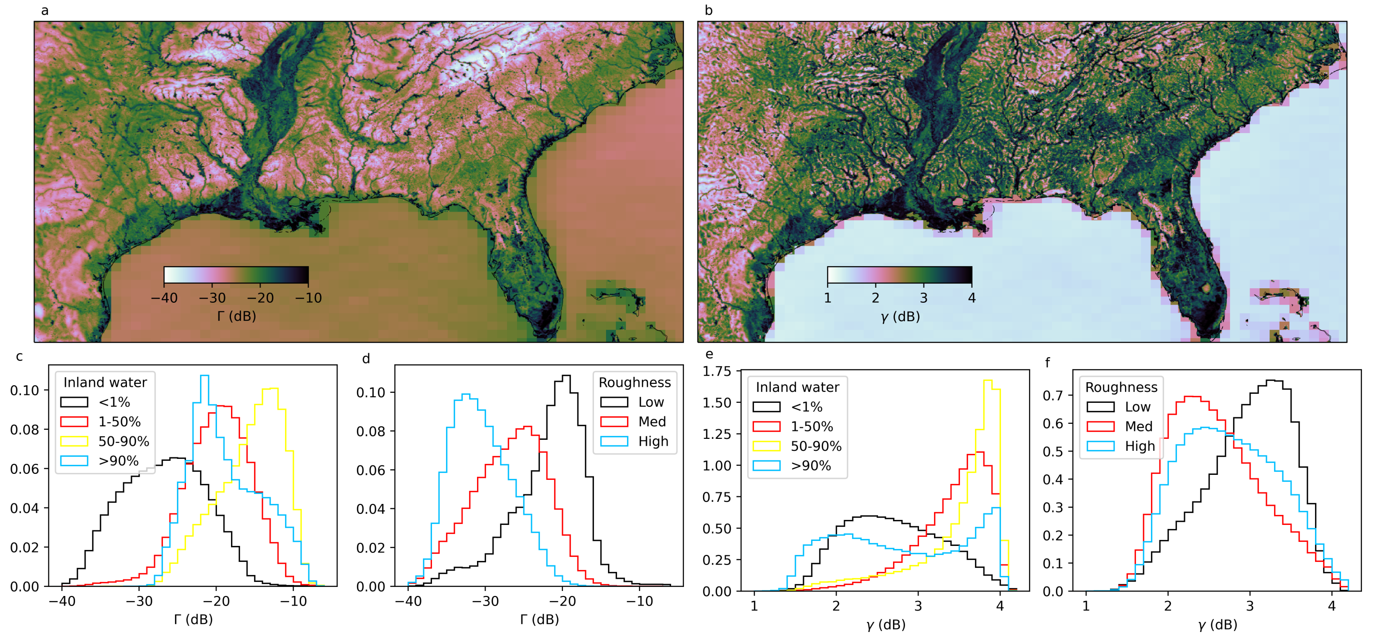

Fig. 4. (a,b) Same as Figure 3(a,c), but constrained to the eastern half of the United States. (c) Distributions of Γ for the entirety of CYGNSS' coverage when binned by surface water fraction. (d) Distributions of Γ when binned by topographic roughness. Low values of roughness are defined when $10\log\sigma <= 5$, medium values when $5 < 10\log\sigma <= 15$, and high values when $10\log\sigma > 15$. (e,f) Same as (c,d), but for γ.

on latitude. Although the spatial footprint of the retrievals is 36 km, researchers have created an interpolated soil moisture product that is gridded to the 9-km EASE-2 grid, (Enhanced L3 Radiometer Global Daily 9 km EASE-Grid Soil Moisture product [34]). We use this product and upsample it to the 3-km EASE-2 grid. For temporal analyses, we define matchups between the SMAP soil moisture retrievals and our DDM metrics to be those which occur in the same 3 km grid cell and on the same calendar day as one another.

4) Vegetation: We upscaled a 1-km pan-tropical biomass dataset described in [35] to our 3-km EASE-2 grid using simple averaging, such that each grid cell is the average biomass of the nine, 1-km grid cells from [35].

III. RESULTS

A. Spatial variations in Γ and γ

Figure 3 shows long term averages of Γ and γ collected between 2020 – 2024 as well as distributions of the two variables when binned by land and ocean. The range of Γ over the ocean surface is smaller than that over land, though the median values are quite similar: the median ocean surface Γ is -26.3 dB, and the median land surface Γ is -25.9 dB. γ shows different behavior, and γ over the ocean is notably lower than γ over the land surface, with the two distributions barely overlapping one another (median ocean surface γ = 1.4 dB, median land surface γ = 2.7 dB). This indicates that power is more spread out in DDMs over the ocean than over land, with smaller peak values relative to power in the surrounding pixels. Similar findings for another DDM coherency metric, leading edge slope, have also been published in [30].

Taking a closer look at γ values over the ocean, astute observers will notice some low frequency variations in γ that look almost like a wrinkled tablecloth. These small variations of 0.2 dB line up directly with the geoid and are likely due to the 0.25 chip sampling of the DDM imperfectly capturing power levels across delay space. This effect has been observed in other DDM studies [36] and is small enough in γ such that it does not significantly affect any of our findings.

Because presenting global figures makes it difficult to visualize smaller details, Figure 4 shows a closer look at Γ and γ over the eastern United States. In this figure, we can see that there are regions where Γ and γ exhibit spatial similarities and differences. For example, both Γ and γ are high over the Mississippi River Basin and both appear high over lakes and rivers throughout the region. However, there are also larger regions with lower Γ where γ is still high. Globally, the spatial correlation between Γ and γ over land is low (r = 0.3), indicating that there are aspects about the land surface that affect Γ and γ differently, in addition to the more stark differences between Γ and γ over the ocean.

B. Drivers of spatial differences in Γ and γ

Here, we describe some of the major drivers affecting the spatial distribution of Γ and γ over the land surface and provide reasons for their similarities and differences.

1) Surface water: The sensitivity of Γ to inland surface water has long been recognized as one of the most significant and noticeable features of GNSS-R observations, and Figure 4c reiterates this same finding. This figure shows how Γ changes with increasing surface water fraction, and as others have found, Γ increases with increased surface water fraction until water almost completely covers the footprint, at which point Γ starts to decrease. This is due to the increase in surface roughness that tends to occur as water bodies grow in size and

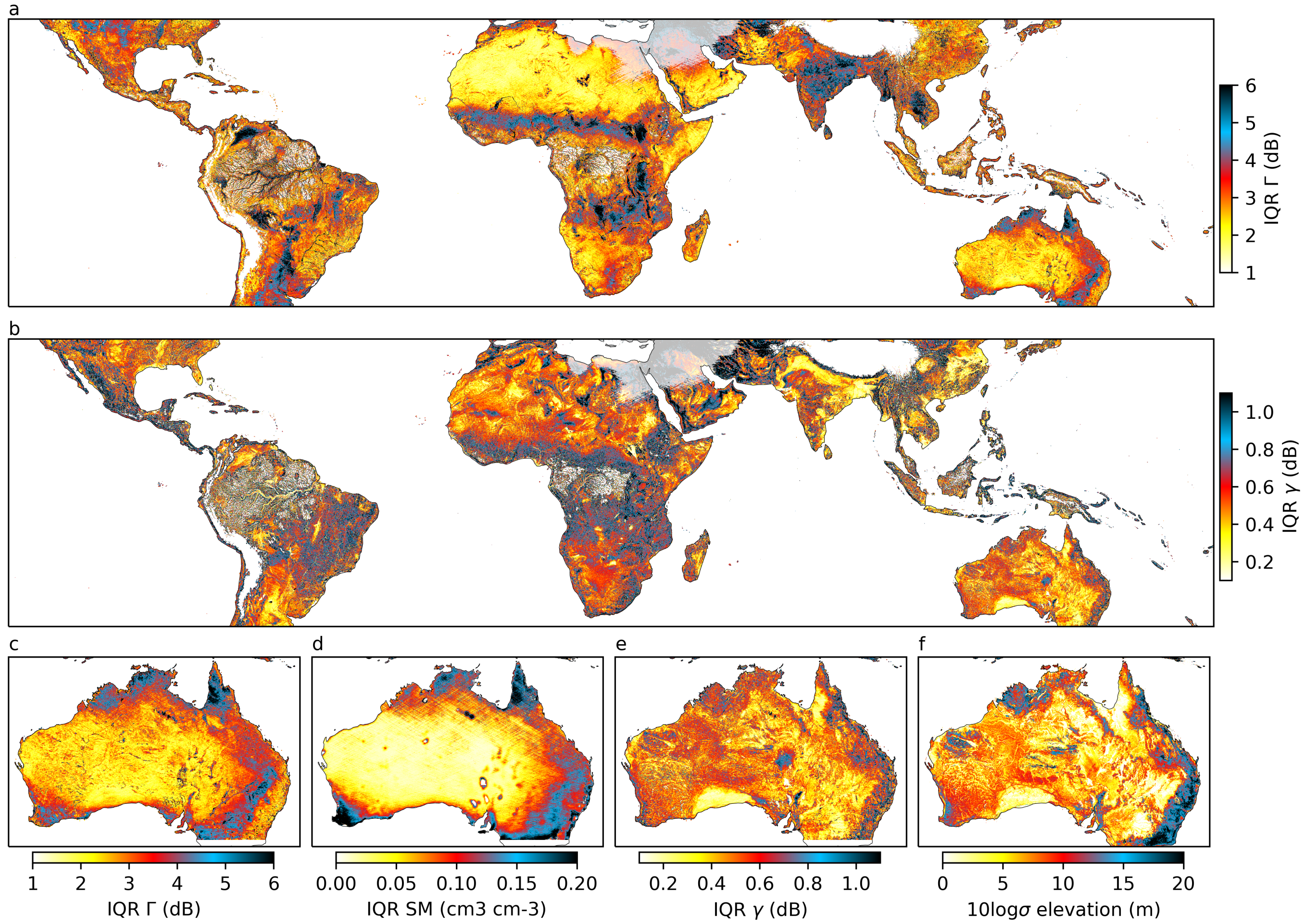

Fig. 5. Inter-quartile ranges (IQR) for Γ (a) and γ (b) calculated using observations between 2020 - 2024. Regions exceeding 3000 m surface elevation have been masked out, and regions in the Middle East that commonly experience RFI are semi-transparent. (c) Same as (a) but only for Australia. (d) IQR of soil moisture for 2020 - 2024 for Australia. (e) Same as (b) but only for Australia. (f) The standard deviation of elevation within each 3 km grid cell for Australia, in dB.

are no longer sheltered from the wind. This same trend is seen in distributions of γ though perhaps even more extreme (Figure 4e). γ increases with increasing surface water fraction only up to a point, after which point it decreases back to its typical value found over dry land, whereas Γ still tends to remain elevated above its dry land value even when surface water fraction exceeds 90 percent. Thus, although thresholding DDM metrics is a common way of deriving binary surface water masks from CYGNSS data, no single global threshold will be able to always accurately identify the presence or absence of surface water using either Γ or γ, particularly for large water bodies.

2) Biomass: Γ and γ respond differently to increased biomass: higher biomass results in lower Γ but higher γ relative to their respective bare soil values. Globally, median Γ over bare soil is -24.8 dB, whereas in areas where biomass exceeds 200 Mg ha-1 it is -33.7 dB. Conversely, median γ over bare soil is 2.5 dB, whereas regions with biomass greater than 200 Mg ha-1 it is 3.3 dB. The Amazon rain forest in South America and dense forests in Central Africa exemplify this effect in Figure 3, where Γ exhibits some of its lowest values globally and, γ, some of its highest.

3) Topography: Topographic roughness, which again is defined as the standard deviation of elevation within a grid cell in dB, affects Γ and γ. Figure 4d,f shows distributions of Γ and γ for low, medium, and high values of topographic roughness, the bins defining which were chosen after qualitatively examining the data and are described in the legend of Figure 4. Both DDM metrics decrease as roughness increases, though there is less separation in the distributions of γ for medium and high roughness values than in Γ.

C. Temporal variations in Γ and γ

Topography can also affect the temporal variability of γ within a grid cell, and this stands in contrast to temporal variability of Γ. Figure 5 shows the inter-quartile ranges (IQRs) of daily averages of Γ (a) and γ (b) for 2020 - 2024. The IQR is defined as the difference between the 75th and 25th percentiles of a dataset and is one of many ways of indicating the magnitude of spread within a dataset, while being less sensitive to outliers than the total range. There are regions, like the Sahara Desert, where Γ does not tend to vary

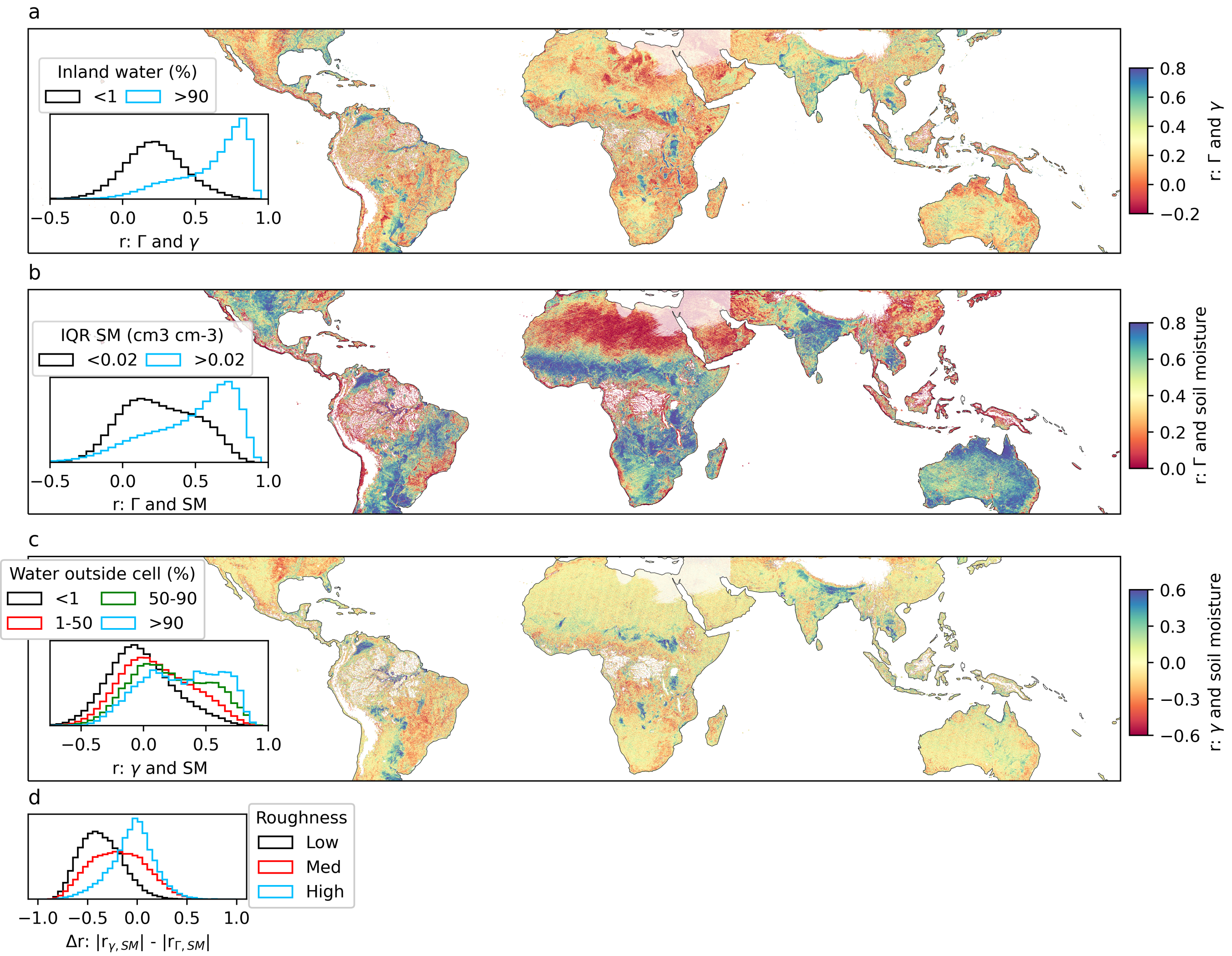

Fig. 6. (a) The correlation between daily matchups of Γ and γ during 2020 - 2024. Inset figure shows distributions of the correlation when there is <1 percent surface water fraction in the grid cell (black) and >90 percent surface water fraction (blue). (b) The correlation between Γ and soil moisture for the same time period. Inset figures shows distributions of the correlation when the observed IQR of soil moisture is $<=0.02$ cm-3 cm-3 (black) and >0.02 cm3 cm-3 (blue). (c) The correlation between γ and soil moisture for the same time period. Inset figure shows distributions of the correlation as surface water fraction in cells surrounding the reflection point increase from <1 percent (black), to 1-50 percent (red), 50-90 percent (green), and >90 percent (blue). (d) Histograms of the difference in the absolute value of the correlation between γ and soil moisture and Γ and soil moisture. In all figures, regions with surface elevation exceeding 3000 m have been masked out, and regions in the Middle East that commonly experience RFI are semi-transparent.

significantly over time (yellow colors) but γ does (reds, blues, and blacks), as well as regions like northern India where Γ varies substantially whereas γ does not.

These relative differences indicate that the primary factors affecting temporal variability of Γ and γ are different. As others have shown previously [5], the temporal variability of Γ mimics the temporal variability of soil moisture, which we also show in Figure 5c,d for Australia. In Australia, regions where the IQR of Γ is high, the IQR of soil moisture is also high, and vice versa. This trend does not hold for the IQR of γ (Figure 5e), where there is not an obvious relationship between soil moisture variability and variability of γ. However, when we plot topographic roughness (Figure 5f) for the same region, we can see a more clear relationship ($r = 0.63$). In regions with low topographic roughness, we see very little variability of γ, and we see higher γ variability in regions with larger topographic roughness. This is an important detail that will be revisited in the Discussion.

Given the differences in IQRs between Γ and γ, one might expect that these two variables themselves are never correlated. In fact, there are many regions where Γ and γ are highly correlated (Figure 6a), and the following sections explain why.

D. Drivers of temporal differences between Γ and γ

1) Surface water: Hydrologists will immediately notice that Γ and γ tend to be highly positively correlated in regions with large surface water extents, either as permanent water bodies or seasonally-inundated wetlands (Figure 6a). And, if we look at the distributions of the correlation for grid cells with less than 1 percent surface water extent vs. cells with greater than 90 percent surface water extent (inset histograms in Figure 6a), we see that this is indeed the case. Recall from our earlier presentation of surface water's effect on mean Γ and γ that usually, once surface water extent exceeds 90 percent, both of the metrics begin to decrease back to their dry soil values (Figure 4c,e). However, this is not the case with the correlation between the two variables–the higher the surface water extent, the greater the correlation between Γ and γ.

2) Soil moisture: As Figure 5c,d alluded to, soil moisture affects Γ and γ differently. Figure 6b,c show the correlation between Γ and soil moisture (b) and γ and soil moisture (c) for 2020 - 2024. Similar statistics to those presented in Figure 6b have been presented before (e.g., [5]), though we repeat it here to contrast with the relationship found with γ. Γ and soil moisture are very often highly positively correlated, with many grid cells exhibiting a greater than 0.8 correlation with soil moisture, and it is for this reason why Γ is often used as the primary variable in GNSS-R soil moisture retrieval algorithms. As others have also found, this high positive correlation exists nearly everywhere that there is some amount of temporal soil moisture variability (inset histograms of Figure 6b), and low correlations tend to be found in regions with nearly no variability in soil moisture.

The relationship between γ and soil moisture is more complex, with both positive, negative, and close to zero correlation found across the landscape (Figure 6c). The highest positive correlations are found where there is both water in the grid cell of interest *and* water in immediately adjacent grid cells (blue distribution in inset figure of Figure 6c). These are very similar to the regions where γ and Γ were also positively correlated (Figure 6a).

The most negative correlations are found in grid cells where there *is* water in the grid cell of interest but *no* water in adjacent grid cells (black distribution in inset figure of Figure 6c). Now, if you are still paying attention, you may be asking yourself, "Why are they talking about water in *adjacent* grid cells?" This and the answer to other questions will be revealed in the Discussion.

But for now, let us focus our attention on one such example. Figure 7a shows the correlation between γ and soil moisture, though now focused on the part of California that CYGNSS observes. Although there are areas of positive, no, and negative correlations, there is a notable red line of negative correlations that transects most of the figure. When we zoom in to satellite imagery of this streak of pixels, we always see that which is shown in Figure 7b: agricultural land on either side of the California aqueduct, which transports water from the Sierra Mountains to Southern California and is, on average, around 50 m wide. Note that the aqueduct is too narrow to be included in any static water maps we could find, including the one we use in this analysis, though it clearly has an effect on the relationship between γ and soil moisture. The correlation between γ and soil moisture for the land captured in Figure 7b is -0.60, which is actually a stronger relationship than that observed for Γ and soil moisture in this location (r = 0.36) (Figure 7(c,d). In other words, at this location, γ is more sensitive to soil moisture than is Γ.

There are thus regions where γ is more sensitive to soil moisture than Γ. The California aqueduct observation naturally leads one to wonder if it is possible to identify the conditions under which γ is likely to be more sensitive to soil moisture than Γ. Given that the IQR of γ has a positive relationship with topographic roughness, we further subset the data shown in the inset of Figure 6c to includes the effects of roughness (Figure 6d). Here, we included the cells that comprised the distribution in black in Figure 6c and further removed cells that had an IQR of soil moisture less than 0.02 cm3 cm-3. We then binned the remaining cells by low, medium, and high values of topographic roughness. The distribution in Figure 6d shows the difference in the absolute value of the correlations between γ and soil moisture and Γ and soil moisture. Negative values indicate a stronger relationship between Γ and soil moisture, and positive values indicate a stronger relationship between γ and soil moisture. As this figure shows, and as we might expect, Γ is more sensitive to soil moisture for the vast majority of regions that CYGNSS observes. However, there are situations where γ is more sensitive, and these areas tend to have at least a moderate level of topographic roughness with water in the grid cell of interest with no water in surrounding grid cells.

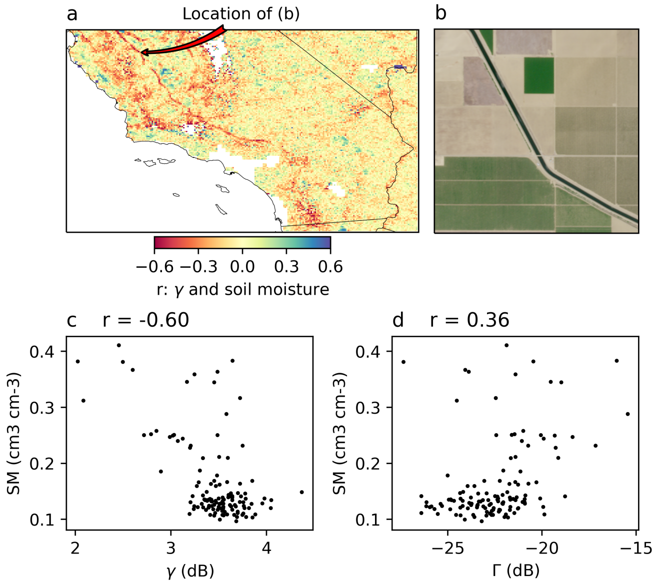

Fig. 7. (a) Same as Figure 6c, but focused on California below 38 degrees latitude. The red arrow indicates the location of the pixel in (b). (b) A Sentinel-2 image of a 3 x 3 km pixel where γ and soil moisture are negatively correlated. The California aqueduct bisects the pixel. Modified Copernicus Sentinel data [2024] processed by the Copernicus Browser. (c) Relationship between γ and soil moisture for the pixel. (d) Relationship between Γ and soil moisture for the same pixel.

IV. Discussion

So far, we have seen that both Γ and γ are sensitive to surface water, topographic roughness, biomass, and soil moisture, though at times these relationships are complex and contradictory to one another. Both Γ and γ increase, and then decrease, as surface water increases, whereas the correlation between them continues to rise. Regions with low topographic roughness are regions with almost no temporal variation in γ, though these areas can have significant variations in Γ. Biomass causes Γ to decrease, but it causes γ to increase.

Finally, soil moisture and its influence on γ is an enigma, with positive, negative, and no relationships. Of course the question is: Why? Now, we will finally explain the drivers behind the behavior of γ and better yet, how we can use it to our advantage.

A. Why γ behaves the way it does

When using DDM bins immediately surrounding Γ, it is important to consider what these bins physically represent and how they could inform our use of the γ metric. Many prior studies such as [37] have thoroughly discussed the mapping between DDM space and physical space. Generally, the DDM bin with the highest power is in the region of the specular point. This bin is used to calculate Γ. Over rough surfaces, such as a wind-roughened ocean or complicated land terrain, a DDM's mapping to physical space will include contributions from a larger 'glistening zone' with power scattered from regions outside of the specular region. The glistening zone results in DDMs containing diffuse scattering contributions in the adjacent DDM bins to the peak power bin, which are used to calculate γ.

Let's go back to our California aqueduct example (Figure 7) and think conceptually about what is happening. As we already explained, in this example there is a weak but positive relationship between Γ and soil moisture, and a strong but negative relationship between γ and soil moisture. This means that the value of the peak pixel increases when soil moisture increases, as we would expect, but in this case the pixels surrounding the peak increase *more* relative to the increase of the peak pixel. This causes the difference between the surrounding pixels and the peak pixel to shrink, i.e., a decreasing γ. For now, let's assume that our surface reflections contain both a specular component and a diffuse component. When soil moisture increases, both the specular and diffuse components will increase due to the increase in dielectric constant. However, if there is any amount of surface water in the specular component, and not as much water in the surrounding, diffuse environment, the sensitivity of the specular component to the change in soil moisture will be *smaller* than the sensitivity of the diffuse component to the same change in soil moisture [38]. In other words, the peak value will not increase as much as the surrounding pixels do when soil moisture increases. This is why we see negative correlations between γ and soil moisture in regions that both: have some roughness (i.e., actually have a diffuse component that causes some spread in DDM power) and have even a small amount of water in the region of the surface contributing to the specular component (i.e., the first Fresnel zone). In these regions, Γ is still sensitive to soil moisture; however, the diffuse component is even more sensitive.

This explains why sometimes γ is negatively correlated with soil moisture, but what about the no and positive correlation scenarios? Any environment where the diffuse and specular components experience the same increase in surface dielectric constant when soil moisture changes will see no change in γ when soil moisture changes and thus zero correlation. A positive correlation of γ and soil moisture, on the other hand, is likely a red herring. In order for γ to increase, the diffuse component must decrease relative to the specular component. The most likely scenario for this to occur is when the land surface floods. And, given that most of the regions where we see positive correlations between γ and soil moisture are in areas that seasonally flood, this seems like a plausible explanation.

These findings are important because they change the way coherency metrics have thus far been interpreted. They cannot be viewed as simply an indicator of the roughness of the reflecting surface. A change in a coherency metric like γ can also solely come from changes in the dielectric constant of the diffuse component relative to the specular component. In Figure 3, we showed distributions of γ over the ocean relative to the land surface. However, just because γ is much lower over the ocean doesn't necessarily mean it's rougher than the land surface. We have to keep in mind that the diffuse component is going to be large over the ocean (because it is rough) but it is also very much full of water, which means the dielectric constant of the diffuse component is also large. If the ocean were as rough as it is but not made of water, and instead made of soil, the diffuse component would be smaller because of the lowered dielectric constant, likely resulting in a larger value of γ.

We can take this argument to its extreme–what happens when the diffuse component is so attenuated that it disappears? We don't have to imagine this scenario, as it likely exists over the dense forests in the Amazon and Central Africa. The vegetation in these areas is so dense that Γ is barely detectable, and the large values of γ mean even lower values of the surrounding pixels, likely indicating a diffuse component that is barely detectable. Somewhat paradoxically, this might mean that the spatial resolution of these areas is actually smaller than if the surface were less rough, as a lack of a diffuse reflection means that any received power only comes from the specular component. In areas with a detectable diffuse component, if this component increases due to an increase in soil moisture, does this effectively mean that moist soils could result in reflections with larger spatial footprints relative to dry soils? Answering this question is outside the scope of this study, though an interesting brain teaser.

B. How do we use γ to our advantage

If we combine information from both Γ and γ, we can better understand the reflecting surface, even if determining the spatial resolution remains challenging. A change in Γ alone, as we already know, can't tell us if soil moisture is changing or if surface water is changing. A change in γ alone also can't tell us if soil moisture or inundation extent are changing. But if we look at both of them together, we should be able to better distinguish the primary driver behind their changes.

Let's turn our attention to one last example from New South Wales, Australia, which experienced long-lasting and significant flooding in the fall of 2022 (Figure 8a-c). A multi-year time series from this location shows the expected increases and decreases in Γ (Figure 8d), which are well correlated with soil moisture (r = 0.72). Though, during the flooding

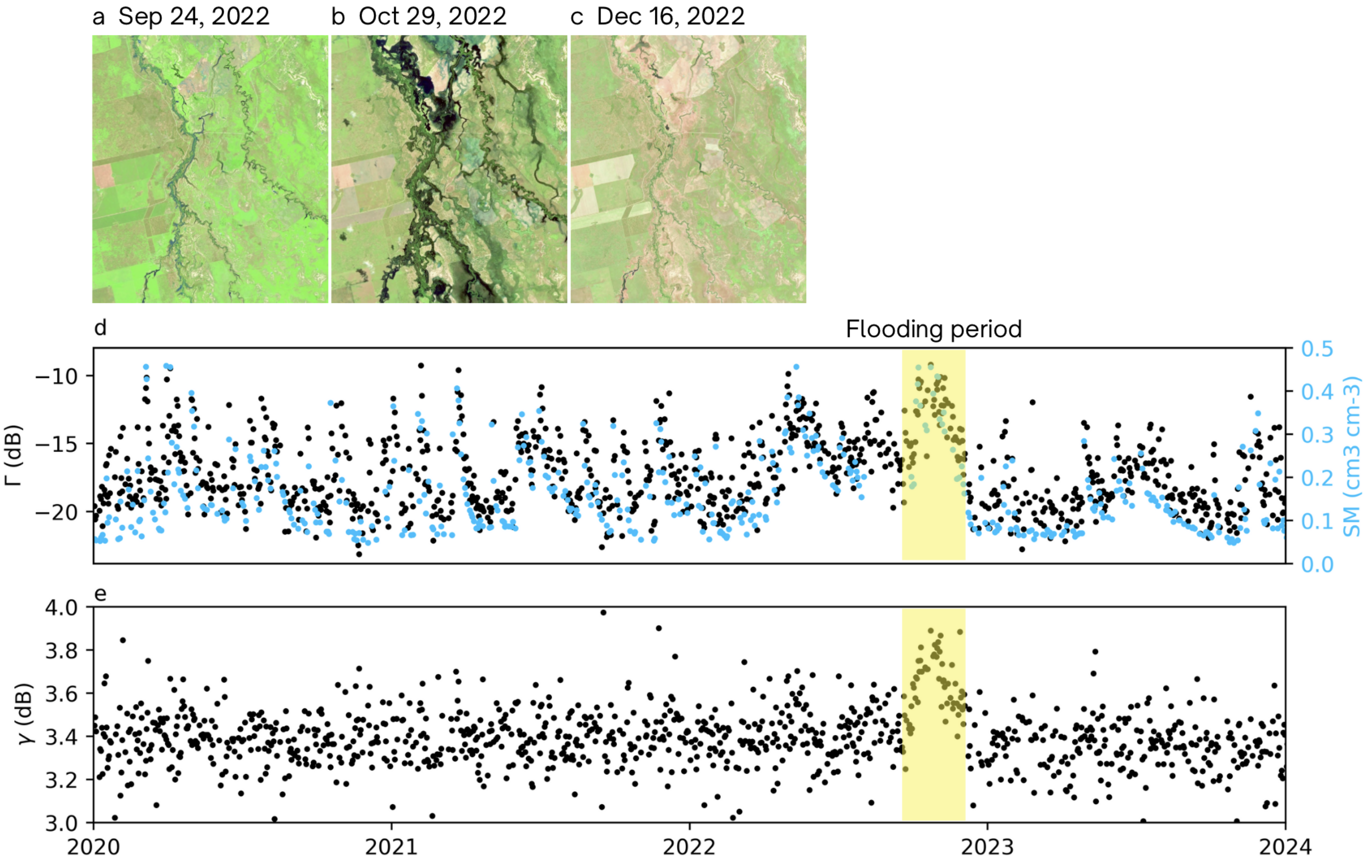

Fig. 8. Shortwave infrared (SWIR) Copernicus Sentinel images [2022] processed by the Copernicus Browser for a region in New South Wales, Australia, before (a), during (b), and after (c) a significant flood event in 2022. (d) Time series of Γ (black) and soil moisture (blue) for this location. (e) Time series of γ for the same location. The yellow semi-transparent box indicates the flooding period.

period, Γ values are not obviously different from those outside of this period, making any surface water identification using Γ alone difficult. When we examine a time series of γ for this location (Figure 8e), for the most part the data appear noisy without any clear correlation with soil moisture or Γ. However, during the flooding period, we see a clear and consistent increase in Γ when the flood waters rise, and an similar decrease as the waters recede. The noise in γ and previous analysis from Figure 4 showing a lack of a single global threshold for surface water also makes surface water identification from γ alone challenging. However, if we look at both Γ and γ together, it is easier to identify the time period when reflections are dominated by soil moisture changes vs. surface water changes. In particular, the correlation between Γ and γ in the four months preceding the flood was only 0.5, whereas the correlation during the months encompassing the flood period increased to nearly 0.8.

If surface water increases, both Γ and γ will increase. This is due to a larger specular component and diminishing diffuse component, since most of the time surface water is smoother than the land it replaces. Conversely, if soil moisture increases, then Γ will increase, but γ could either increase or decrease depending on the amount of surface water within the specular component. If there is water in the specular component, then γ will decrease when soil moisture increases. If there isn't water in the specular component, then the diffuse and specular components will increase the same amount due to the change in the surface dielectric constant, leading to no change in γ and no correlation with soil moisture (e.g., most of Australia in Figure 6c).

Put simply, if both Γ and γ increase, we can be confident that surface water has increased. If Γ increases and γ decreases or stays the same, then we know soil moisture has increased. With the addition of γ, we can begin to identify the primary driver behind changes in our GNSS-R observations.

V. CONCLUSION

In this paper we presented a new DDM metric, γ, and compared it with the ever popular Γ. Although similar in many respects, key differences in Γ and γ could help us distinguish whether our reflecting surface is flooding or simply changing its soil moisture content. Identifying the specific data processing techniques, spatiotemporal aggregation schema, or correlation thresholds for optimizing the distinction between changes in soil moisture and surface water is outside the scope of this study, but we hope this work will encourage others to explore combining DDM metrics to better understand the conditions of the reflecting surface. And perhaps more importantly, we hope our work will motivate other researchers to also dig through the trash to find more hidden gems in GNSS-R data in order to push the technique forward.

ACKNOWLEDGMENT

This work was funded by the NASA Early Career Research Program award number 80NSSC23K0849 and the CYGNSS Extended Mission Phase E. The authors would like to thank those on the CYGNSS team for providing the highest quality GNSS-R dataset possible.

REFERENCES

[1] C. Ruf, S. Gleason, A. Ridley, R. Rose, and J. Scherrer, "The nasa cygnss mission: Overview and status update," in *2017 IEEE International Geoscience and Remote Sensing Symposium (IGARSS)*, 2017, pp. 2641–2643.

[2] C. Ruf, C. Chew, T. Lang, M. Morris, K. Nave, A. Ridley, and R. Balasubramaniam, "A new paradigm in earth environmental monitoring with the cygnss small satellite consteallation," *Scientific Reports*, vol. 8, p. 8782, 2018.

[3] M. P. Clarizia, N. Pierdicca, F. Costantini, and N. Floury, "Analysis of cygnss data for soil moisture retrieval," *IEEE Journal of Selected Topics in Applied Earth Observations and Remote Sensing*, vol. 12, no. 7, pp. 2227–2235, 2019.

[4] M. M. Al-Khaldi, J. T. Johnson, A. J. O'Brien, A. Balenzano, and F. Mattia, "Time-series retrieval of soil moisture using cygnss," *IEEE Transactions on Geoscience and Remote Sensing*, vol. 57, no. 7, pp. 4322–4331, 2019.

[5] C. C. Chew and E. E. Small, "Soil moisture sensing using spaceborne gnss reflections: Comparison of cygnss reflectivity to smap soil moisture," *Geophysical Research Letters*, vol. 45, no. 9, pp. 4049–4057, 2018. [Online]. Available: https://agupubs.onlinelibrary.wiley.com/doi/abs/10.1029/2018GL077905

[6] H. Kim and V. Lakshmi, "Use of cyclone global navigation satellite system (cygnss) observations for estimation of soil moisture," *Geophysical Research Letters*, vol. 45, no. 16, pp. 8272–8282, 2018. [Online]. Available: https://agupubs.onlinelibrary.wiley.com/doi/abs/10.1029/2018GL078923

[7] V. Senyurek, F. Lei, D. Boyd, M. Kurum, A. C. Gurbuz, and R. Moorhead, "Machine learning-based cygnss soil moisture estimates over ismn sites in conus," *Remote Sensing*, vol. 12, no. 7, 2020. [Online]. Available: https://www.mdpi.com/2072-4292/12/7/1168

[8] F. Lei, V. Senyurek, M. Kurum, A. C. Gurbuz, D. Boyd, R. Moorhead, W. T. Crow, and O. Eroglu, "Quasi-global machine learning-based soil moisture estimates at high spatio-temporal scales using cygnss and smap observations," *Remote Sensing of Environment*, vol. 276, p. 113041, 2022. [Online]. Available: https://www.sciencedirect.com/science/article/pii/S0034425722001559

[9] M. M. Nabi, V. Senyurek, A. C. Gurbuz, and M. Kurum, "Deep learning-based soil moisture retrieval in conus using cygnss delay–doppler maps," *IEEE Journal of Selected Topics in Applied Earth Observations and Remote Sensing*, vol. 15, pp. 6867–6881, 2022.

[10] Q. Yan, W. Huang, S. Jin, and Y. Jia, "Pan-tropical soil moisture mapping based on a three-layer model from cygnss gnss-r data," *Remote Sensing of Environment*, vol. 247, p. 111944, 2020. [Online]. Available: https://www.sciencedirect.com/science/article/pii/S003442572030314X

[11] M. M. Al-Khaldi, J. T. Johnson, S. Gleason, C. C. Chew, C. Gerlein-Safdi, R. Shah, and C. Zuffada, "Inland water body mapping using cygnss coherence detection," *IEEE Transactions on Geoscience and Remote Sensing*, vol. 59, no. 9, pp. 7385–7394, 2021.

[12] P. T. Setti and S. Tabibi, "Spaceborne gnss-reflectometry for surface water mapping in the amazon basin," *IEEE Journal of Selected Topics in Applied Earth Observations and Remote Sensing*, vol. 17, pp. 6658–6670, 2024.

[13] T. Pu, C. Gerlein-Safdi, Y. Xiong, M. Li, E. A. Kort, and A. A. Bloom, "Berkeley-rwawc: A new cygnss-based watermask unveils unique observations of seasonal dynamics in the tropics," *Water Resources Research*, vol. 60, no. 7, p. e2024WR037060, 2024. [Online]. Available: https://agupubs.onlinelibrary.wiley.com/doi/abs/10.1029/2024WR037060

[14] P. Zeiger, F. Frappart, J. Darrozes, C. Prigent, and C. Jiménez, "Analysis of cygnss coherent reflectivity over land for the characterization of pan-tropical inundation dynamics," *Remote Sensing of Environment*, vol. 282, p. 113278, 2022. [Online]. Available: https://www.sciencedirect.com/science/article/pii/S0034425722003844

[15] C. Chew, E. Small, and H. Huelsing, "Flooding and inundation maps using interpolated cygnss reflectivity observations," *Remote Sensing of Environment*, vol. 293, p. 113598, 2023. [Online]. Available: https://www.sciencedirect.com/science/article/pii/S0034425723001499

[16] M. Asgarimehr, D. Entekhabi, and A. Camps, "Diurnal vegetation moisture cycle in the amazon and response to water stress," *Geophysical Research Letters*, vol. 51, no. 19, p. e2024GL111462, 2024, e2024GL111462 2024GL111462. [Online]. Available: https://agupubs.onlinelibrary.wiley.com/doi/abs/10.1029/2024GL111462

[17] H. Carreno-Luengo, G. Luzi, and M. Crosetto, "Above-ground biomass retrieval over tropical forests: A novel gnss-r approach with cygnss," *Remote Sensing*, vol. 12, no. 9, 2020. [Online]. Available: https://www.mdpi.com/2072-4292/12/9/1368

[18] X. Wu, P. Guo, Y. Sun, H. Liang, X. Zhang, and W. Bai, "Recent progress on vegetation remote sensing using spaceborne gnss-reflectometry," *Remote Sensing*, vol. 13, no. 21, 2021. [Online]. Available: https://www.mdpi.com/2072-4292/13/21/4244

[19] G. Pilikos, M. P. Clarizia, and N. Floury, "Biomass estimation with gnss reflectometry using a deep learning retrieval model," *Remote Sensing*, vol. 16, no. 7, 2024. [Online]. Available: https://www.mdpi.com/2072-4292/16/7/1125

[20] E. Santi, S. Paloscia, S. Pettinato, G. Fontanelli, M. P. Clarizia, D. Comite, L. Dente, L. Guerriero, N. Pierdicca, and N. Floury, "Remote sensing of forest biomass using gnss reflectometry," *IEEE Journal of Selected Topics in Applied Earth Observations and Remote Sensing*, vol. 13, pp. 2351–2368, 2020.

[21] D. Comite, L. Cenci, A. Colliander, and N. Pierdicca, "Monitoring freeze-thaw state by means of gnss reflectometry: An analysis of techdemosat-1 data," *IEEE Journal of Selected Topics in Applied Earth Observations and Remote Sensing*, vol. 13, pp. 2996–3005, 2020.

[22] H. Carreno-Luengo, C. S. Ruf, S. Gleason, and A. Russel, "Capturing soil surface freeze dynamics over the arctic-boreal zone with gnss-reflectometry," *IEEE Transactions on Geoscience and Remote Sensing*, pp. 1–1, 2025.

[23] C. Chew, S. Lowe, N. Parazoo, S. Esterhuizen, S. Oveisgharan, E. Podest, C. Zuffada, and A. Freedman, "Smap radar receiver measures land surface freeze/thaw state through capture of forward-scattered l-band signals," *Remote Sensing of Environment*, vol. 198, pp. 333–344, 2017. [Online]. Available: https://www.sciencedirect.com/science/article/pii/S003442571730278X

[24] R. De Roo and F. Ulaby, "Bistatic specular scattering from rough dielectric surfaces," *IEEE Transactions on Antennas and Propagation*, vol. 42, no. 2, pp. 220–231, 1994.

[25] M. T. Hallikainen, F. T. Ulaby, M. C. Dobson, M. A. El-rayes, and L.-k. Wu, "Microwave dielectric behavior of wet soil-part 1: Empirical models and experimental observations," *IEEE Transactions on Geoscience and Remote Sensing*, vol. GE-23, no. 1, pp. 25–34, 1985.

[26] J. Shi, K. Chen, Q. Li, T. Jackson, P. O'Neill, and L. Tsang, "A parameterized surface reflectivity model and estimation of bare-surface soil moisture with l-band radiometer," *IEEE Transactions on Geoscience and Remote Sensing*, vol. 40, no. 12, pp. 2674–2686, 2002.

[27] CYGNSS, "Cygnss level 1 science data record version 3.2," 2024. [Online]. Available: https://podaac.jpl.nasa.gov/dataset/CYGNSS_L1_V3.2

[28] M. J. Brodzik, B. Billingsley, T. Haran, B. Raup, and M. H. Savoie, "Ease-grid 2.0: Incremental but significant improvements for earth-gridded data sets," *ISPRS International Journal of Geo-Information*, vol. 1, no. 1, pp. 32–45, 2012. [Online]. Available: https://www.mdpi.com/2220-9964/1/1/32

[29] C. Chew, T. M. Roberts, and S. Lowe, "Rfi mapped by spaceborne gnss-r data," *NAVIGATION: Journal of the Institute of Navigation*, vol. 70, no. 4, 2023. [Online]. Available: https://navi.ion.org/content/70/4/navi.618

[30] Z. Dong and S. Jin, "Evaluation of the land gnss-reflected ddm coherence on soil moisture estimation from cygnss data," *Remote Sensing*, vol. 13, no. 4, 2021. [Online]. Available: https://www.mdpi.com/2072-4292/13/4/570

[31] v. . Land Cover 2019, "European union's copernicus land monitoring service information," 2019.

[32] E. Podest and W. Crow, "Soil moisture active passive (smap) ancillary data report digital elevation model," 2013. [Online]. Available: https://smap.jpl.nasa.gov/system/internal_resources/details/original/285_043_dig_elev_mod.pdf

[33] J. Peng, P. Mohammed, J. Chaubell, S. Chan, S. Kim, N. Das, S. Dunbar, R. Bindlish, and X. Xu, "Soil moisture active passive (smap) l1-l3 ancillary static data, version 1," 2019. [Online]. Available: http://nsidc.org/data/SMAP_L1_L3_ANC_STATIC/versions/1

[34] P. ONeill, S. Chan, E. Njoku, T. Jackson, R. Bindlish, J. Chaubell, and A. Colliander, "Smap enhanced l3 radiometer global and polar grid daily 9 km ease-grid soil moisture, version 6," 2023. [Online]. Available: http://nsidc.org/data/SPL3SMP_E/versions/6

[35] V. Avitabile, M. Herold, G. B. M. Heuvelink, S. L. Lewis, O. L. Phillips, G. P. Asner, J. Armston, P. S. Ashton, L. Banin, N. Bayol, N. J. Berry, P. Boeckx, B. H. J. de Jong, B. DeVries, C. A. J. Girardin, E. Kearsley, J. A. Lindsell, G. Lopez-Gonzalez, R. Lucas, Y. Malhi, A. Morel, E. T. A. Mitchard, L. Nagy, L. Qie, M. J. Quinones, C. M. Ryan, S. J. W. Ferry, T. Sunderland, G. V. Laurin, R. C. Gatti, R. Valentini, H. Verbeeck, A. Wijaya, and S. Willcock, "An integrated pan-tropical biomass map using multiple reference datasets," *Global Change Biology*, vol. 22, no. 4, pp. 1406–1420, 2016. [Online]. Available: https://onlinelibrary.wiley.com/doi/abs/10.1111/gcb.13139

[36] F. Saïd, Z. Jelenak, P. S. Chang, and S. Soisuvarn, "An assessment of cygnss normalized bistatic radar cross section calibration," *IEEE Journal of Selected Topics in Applied Earth Observations and Remote Sensing*, vol. 12, no. 1, pp. 50–65, 2019.

[37] I. Collett, "Applying gnss reflectometry-based stare processing to modeling and remote sensing of wind-driven ocean surface roughness," Ph.D. dissertation, University of Colorado Boulder, 2021.

[38] C. Chew and E. Small, "Estimating inundation extent using cygnss data: A conceptual modeling study," *Remote Sensing of Environment*, vol. 246, p. 111869, 2020. [Online]. Available: https://www.sciencedirect.com/science/article/pii/S003442572030239X

Clara Chew Clara Chew is a terrestrial hydrologist who specializes in land surface applications of GNSS-Reflectometry. She received her BA from Dartmouth College in 2009 and a PhD in Geology from the University of Colorado Boulder in 2015.

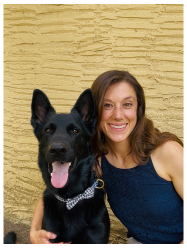

Margaret Scott Margaret Scott is a PhD student at the University of Colorado Boulder studying Aerospace Engineering with a focus in Remote Sensing. She received her BS in Electrical Engineering from Montana State University in 2019 and MS in Aerospace Engineering from the University of Colorado Boulder in 2023.

Ian Colwell Ian Colwell is a data scientist at Muon Space. He received his BS from Westminster University in 2010 and his MS in Analytics from Northwestern in 2014.